Remote Sensing of Environment 174 (2016) 134–147

Contents lists available at ScienceDirect

Remote Sensing of Environment

journal homepage: www.elsevier.com/locate/rse

A physics-based method for the remote sensing of seagrasses

John Hedley [a,*], Brandon Russell [b], Kaylan Randolph [b], Heidi Dierssen [b]

[a] Environmental Computer Science Ltd., Raymond Penny House, Tiverton, Devon EX16 6LR, United Kingdom
[b] Department of Marine Sciences, University of Connecticut, Groton, CT 06340, USA

ARTICLE INFO

Article history:
Received 12 August 2015
Received in revised form 24 November 2015
Accepted 3 December 2015
Available online 18 December 2015

Keywords:
Seagrass
Radiative transfer model
Inversion
Leaf area index
LAI
Uncertainty

ABSTRACT

Seagrass meadows are important environments for the blue carbon budget and are potential early indicators for environmental change. Remote sensing is a viable monitoring tool for spatially extensive meadows but most current approaches are limited by the requirement for in situ calibration data or provide categorical level maps rather than quantitative estimates of direct physiological significance. In this paper we present a method for mapping water depth and the leaf area index (LAI, ratio of leaf area to substrate area) of *Thalassia testudinum* meadows, based on radiative transfer model inversion using an embedded three-dimensional aquatic canopy model. Variations in reflectance due to leaf length, leaf position, sediment coverage on leaves, water depth and solar zenith angle were included in the model to parameterise uncertainty propagation. The model revealed canopy reflectance as a function of LAI decreases exponentially at all wavelengths up to an LAI around four, beyond which increasing canopy density cannot be determined from reflectance. In addition, sediment coverage on leaves has surprisingly little effect on the reflectance of sparse canopies because shading is also a contributor to darkening. The capability of the method for image based mapping was assessed through sensitivity analyses and by application to hyperspectral airborne imagery of Florida Bay collected by the Portable Remote Imaging Spectrometer (PRISM), with the uncertainty propagation providing per-pixel confidence intervals on all the estimated parameters. Results were consistent across the sensitivity and image analyses and the agreement with field data was good, given the challenges in validation of submerged pixels at metre scale. Uncertainties were high for LAIs greater than two in water of depth 8 m, but lower for sparse canopies and shallower water. For water depths approaching 10 m the pixel-to-pixel variation arising from processes at the water surface upwards was greater than the uncertainties arising from the canopy or water column.

The physics-based model inversion approach is readily adaptable to any sensor configuration and to different seagrass species and canopy morphologies. No site-specific in situ data is required and the uncertainty estimates can provide an objective basis for interpreting apparent changes in the distribution of seagrasses over time and space, as revealed by remote sensing techniques.

1. Introduction

Seagrasses are highly productive environments and an important component of the 'blue carbon' budget (Fourqurean et al., 2012; Lavery, Mateo, Serrano, & Rozaimi, 2013). Species such as *Thalassia testudinum* can form extensive meadows over many square kilometres, storing organic carbon in sub-surface rhizomes and the underlying soil (Fourqurean et al., 2012) and contributing to inorganic lime mud through calcification (Enríquez & Schubert, 2014) while also playing a role in carbonate dissolution (Burdige & Zimmerman, 2002). In addition to carbon storage, seagrasses perform many valuable ecosystem services: coastal protection through sediment stabilisation and wave attenuation (Fonseca & Cahalan, 1992); nursery habitats to coral reef fish (Nagelkerken et al., 2002) and feeding grounds for dugongs (Aragones, Lawler, Foley, et al., 2006). Mapping and monitoring of seagrasses is a crucial component of environmental management and is recognised as such in legislature such as the Water Framework Directive in Europe (Gobert et al., 2009). Species such as *T. testudinum* or *Posidonia oceanica* can form meadows over areas of 100's km^2, so remote sensing is an obvious tool for practical monitoring. Changes in meadows can be indicators of sediment transport patterns (Marbà & Duarte, 1995) or environmental changes. Environmental degradation may be visible in seagrass beds by remote sensing long before the consequences for associated environments such as coral reefs are detectable.

Numerous studies have assessed remote sensing for mapping metrics of seagrasses related to canopy density, such as biomass (Knudby & Nordlund, 2011), standing crop (Mumby, Green, Edwards, & Clark, 1997), horizontal projected foliage (Lyons, Phinn, & Roelfsema, 2012), or even to the level of species identification (Phinn, Roelfsema, Dekker, Brando, & Anstee, 2008). To identify trends and change events requires time series monitoring over both short and long term time scales to establish the baselines for natural variability. Lyons et al. (2012), Lyons, Roelfsema, and Phinn (2013) demonstrated inter- and intra-annual

* Corresponding author.
E-mail address: j.d.hedley@envirocs.com (J. Hedley).

http://dx.doi.org/10.1016/j.rse.2015.12.001
0034-4257/

seagrass temporal and spatial dynamics using object-orientated mapping techniques and Landsat imagery. However, object-orientated or per-pixel classification techniques (Blakey, Melesse, & Hall, 2015) suffer from several drawbacks. Firstly they provide discrete classes such as 'low', 'medium' or 'high' density, whereas a quantitative canopy-scale descriptor such as leaf area index (LAI, the ratio of one-sided leaf area to the substrate area covered) would be more directly relatable to ecophysiological parameters or photobiology, which may be required to correctly interpret apparent changes (Lambers, Chapin, & Pons, 2008; Hedley, McMahon, & Fearns, 2014). Regression methods (Mumby et al., 1997; Knudby & Nordlund, 2011) can provide quantitative estimates but require in situ data for calibration and so are limited to situations where this is available. In one recent example Roelfsema et al. (2014) used multispectral satellite data and object-orientated classification to produce a time series of maps of seagrass cover at landscape scale (>100 km^2) with median 52% accuracy for four cover categories. However this analysis utilised around 20,000 manually assessed benthic photos collected over 9 years. The vast majority of sites do not benefit from this level of long term survey data. Another disadvantage of classification and object-orientated methodologies is that they are to some extent 'black boxes', in that the actual physical basis (in terms of radiative transfer) or thresholds that determine the classification are not readily known or interpretable. For example, a time series of maps will typically show regions changing from one class to another; but it can be difficult to assess if these changes are real or due to some other perturbation (for example in the water column) that tips the classification over a threshold in certain locations. In this sense the methods are not very 'auditable': the scope to understand how the result at each pixel is arrived at, or to provide an uncertainty budget, is very low. Even where good results have been demonstrated at sites that are well studied (Lyons et al., 2013) the transferability to other sites where less data is available would be hard to assess. Lack of in situ data for validation or calibration is in general a major challenge for large scale mapping (100's km^2) or retrospective time series analysis (Wabnitz, Andréfouët, Torres-Pulliza, Müller-Karger, & Kramer, 2008).

An alternative to the above approaches is that of shallow-water mapping algorithms based on radiative transfer model inversion, sometimes called 'physics-based' methods (Dekker et al., 2011). These methods establish a parameterised model of the spectral reflectance as measured by the sensor based on a physical model of light propagation through the system of interest. In principle this enables the derivation of bathymetry, water column optical properties and bottom reflectance without the need for in situ data. Clearly there are unknowns or uncertainties in the system, but providing the possible ranges are adequately characterised these can form the basis of an uncertainty propagation and be documented as error bars on the associated estimations at each pixel (Hedley, Roelfsema, & Phinn, 2010; Hedley, Roelfsema, Koetz, & Phinn, 2012). In the work presented here we have embedded a *Thalassia* canopy model (Hedley & Enríquez, 2010) into the typical form of a shallow-water inversion model (Hedley, Roelfsema, & Phinn, 2009), such that LAI is estimated at each pixel in conjunction with bathymetry and other parameters. The relationship between canopy LAI and reflectance is not precise: the same LAI can give rise to different canopy reflectances, due to factors such as the

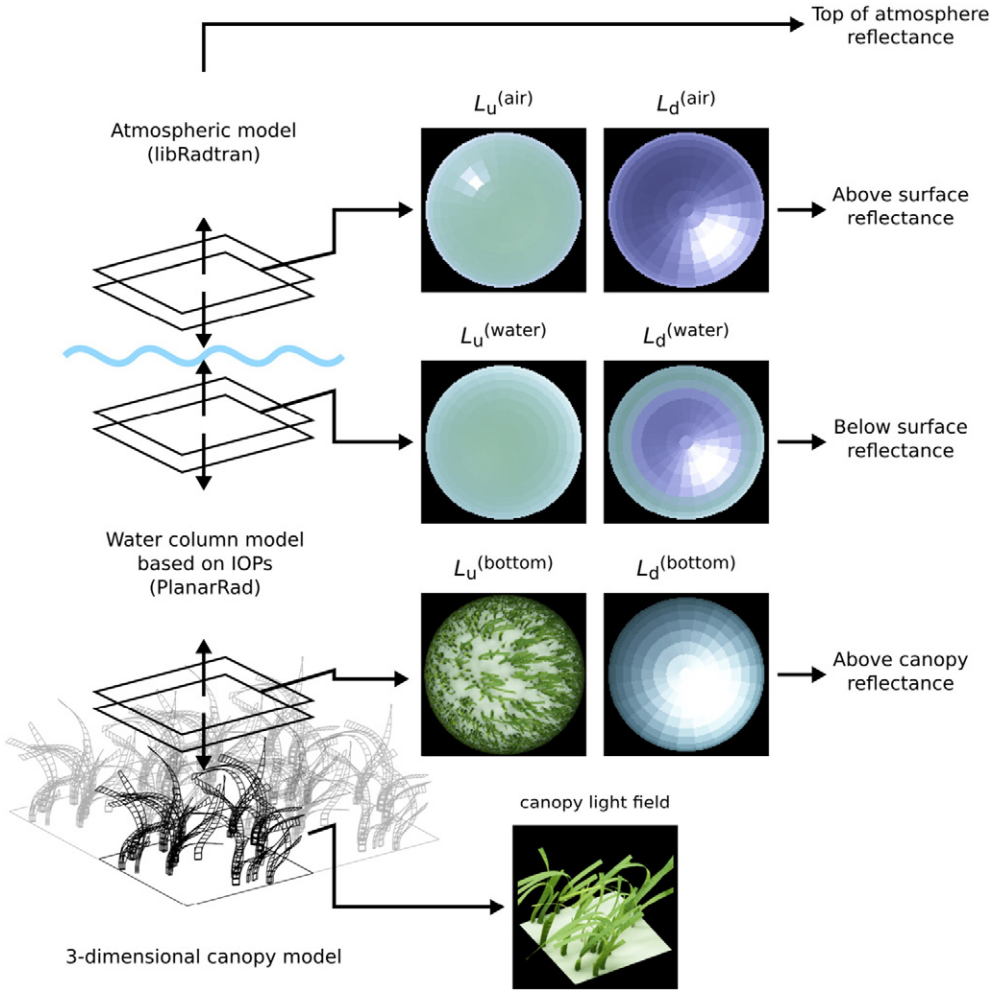

Fig. 1. Radiative transfer model framework consisting of a coupled canopy model, water column model and atmospheric model. Above canopy reflectance is the primary output utilised in the work presented here.

distribution of leaf lengths, leaf positions, sediment and epiphytes on leaves, or the interaction of the bi-directional reflectance distribution function (BRDF) with the incident light field. Using the canopy model we have characterised these variations and built them into the algorithm, such that they are part of the budget of the uncertainty propagation. The resulting method has the potential to overcome some of the drawbacks of the previously discussed approaches. Being based on a physical model the estimated LAI is traceable through intermediate values that are easily interpretable, such as the bottom of water column reflectance. The per-pixel uncertainty propagation provides a basis to understand if apparent changes over time are within the capability of the method to determine.

The work was structured as follows 1) the canopy model was used to investigate how different aspects of canopy morphology contribute to variation in canopy reflectance; 2) the canopy model was simplified and embedded into a shallow-water mapping algorithm; 3) the capability of the algorithm was assessed by a sensitivity analysis, and 4) by application to hyperspectral airborne imagery of seagrass meadows in Florida Bay, USA. In the final section of the paper the implications for applying the method to other imagery sources such as multispectral satellite data are discussed.

2. Methods

2.1. Overview

The methodological steps consisted of: 1) A three-dimensional canopy model was used to generate a large database of top of canopy reflectances for a canopies with various parameters of LAI, leaf length, leaf position, and leaf sediment load; 2) The database was queried to provide insight into the significance of the different factors in contributing to uncertainty in the relationship between LAI and reflectance; 3) Principal components analysis and regression was used on the database to produce a simplified functional form for top of canopy spectral reflectance as a function of LAI and one or more uncertainty terms; 4) The top of canopy reflectance function was embedded into the shallow water mapping algorithm of Lee, Carder, Mobley, Steward, and Patch (1998, 1999) and a sensitivity analysis based on image noise was used to investigate LAI detectability as a function of depth; 5) Finally, the LAI algorithm was applied to hyperspectral airborne data of *Thalassia* beds in the Florida keys and the LAI estimates were compared to in situ survey data (for brevity *Thalassia* is used to refer to *T. testudinum* throughout). The following sections provide details on each component.

2.2. Radiative transfer modelling

An existing radiative transfer model for seagrass canopies (Hedley, 2008; Hedley & Enríquez, 2010; Hedley et al., 2014) was used to model the reflectance just above the top of the canopy (Fig. 1). The model is fully three-dimensional, the leaf positions are determined by a physical dynamic model for leaf bending under a simple wave force model, allowing canopies to assume naturalistic positions from upright to flattened (Fig. 2). Canopies were modelled at a scale of 30 × 30 cm for LAIs from 0.1 to 10 in 15 sets, each set consisted of three leaf length treatments, long (L), medium (M) and short (S), each in four positions: two described as relatively 'flattened' vs. two 'upright' (see examples in Fig. 2). Leaves were arranged in shoots of 2, 3 or 4 leaves and for the medium length treatment the mean leaf length was 12 cm with a standard deviation of 6.0 cm, for the short treatment the mean and standard deviation were halved and for the long treatment they were doubled. The leaf length distributions were chosen to be comparable to actual canopy data (Hedley & Enríquez, 2010), but with a simple form of variation between the treatments that could be easily and generally interpreted (as opposed to restricting the results to metrics of actual canopies). Five random repeats were generated for all canopy structure combinations in order to provide a substantial dataset (Table 1).

For simplicity *Thalassia* leaf spectral reflectance and absorptance were assumed constant along the leaf lengths and were derived from the reflectance and absorbance spectra reported in Zimmerman (2003) (Fig. 3b). The method of converting absorbance (a logarithmic quantity as reported by spectrophotometer) to absorptance (the absorbed proportion of the total light incident onto a leaf surface) is given in Hedley and Enríquez (2010). The inclusion of reflectance variation between and within-leaves was considered out of scope for this work, although it can be accommodated by the canopy model (Hedley & Enríquez, 2010). Five different sediment reflectances were employed (Table 1, Fig. 3a), four from the Great Bahama Bank (Dierssen, Zimmerman, Drake, & Burdige, 2010) and one from a data set collected

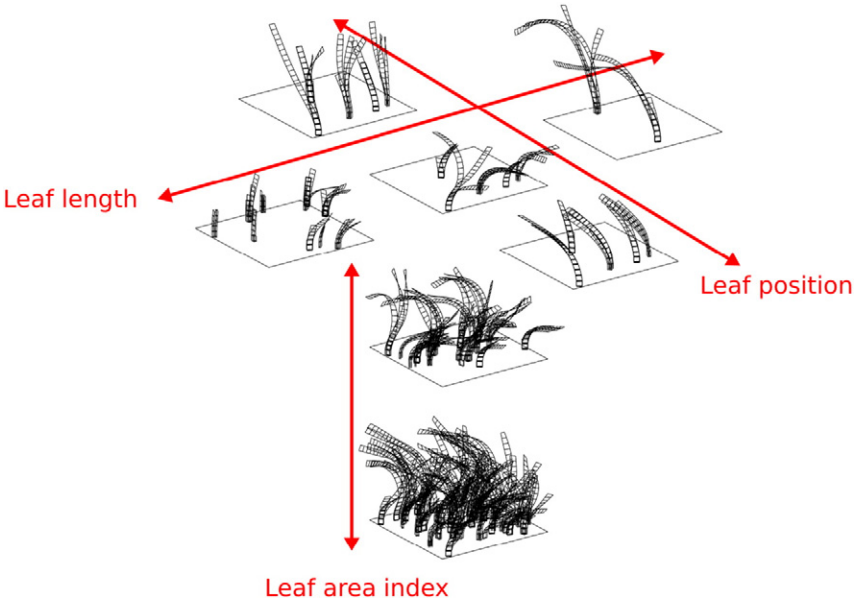

Fig. 2. Three factor experimental design for variation in canopy structure, for a given LAI (vertical position) canopy structure can be varied in terms of the distribution of leaf lengths and also by leaf position (horizontal axes).

Table 1
Experimental design of model runs for establishing the variation of above canopy diffuse reflectance with LAI and other factors (note SZA is solar zenith angle). The final database contained 43,200 spectral reflectances.

	Leaf length	LAI	Position	Sand reflectance	Leaf reflectance	SZA	Depth	Random repeats	Total
n	×3	×15	×4	×5	×1 or ×3	×2	×3	×5	43,200
	S M L	0.1 to 10	2 upright 2 flattened	Andros Palau North Exuma Grapestone	Clean 10%, 25% sediment covered (only with North sand)	26° 56°	1 m 5 m 10 m		

in Palau, Micronesia (Hedley, Mumby, Joyce, & Phinn, 2004). The intention was to provide a methodology that could be applied under a wide range of sediment brightness. The Palau and 'North' sediment reflectance profiles were very similar (Fig. 3a), the North reflectance was used in the majority of the subsequent analysis. At the site where remotely sensed data was acquired the *Thalassia* leaves were frequently partially covered in sediment (Fig. 4) so two additional treatments included modifying the leaf reflectance and transmittance equivalent to 10% and 25% coverage by sediment (Table 1). This was simulated by making the leaf reflectance a linear mix of leaf and sediment reflectance in ratios 9:1 and 4:1 and adjusting the leaf transmittance at each wavelength such that the ratio of transmittance to transmittance plus absorptance was preserved. The maximum of 25% leaf sedimentation was visually estimated from photographs of the canopies (Fig. 4). In practice, individual leaves could be clear of sediment or almost completely covered, 25% was estimated as a reasonable average figure for the most sediment laden images.

The canopy model was parameterised to calculate in 16 spectral bands of 20 nm width over the range 400 to 720 nm. All reflectances were resampled to these bands, the effect of which was only to smooth the smallest spectral features (Fig. 3a vs. Fig. 4). This smoothing is relatively inconsequential to the subsequent analyses which minimise the least-squares fit over the whole spectral shape.

In this application the model was used to calculate the diffuse reflectance above the canopy at fixed height of 27 cm above the sediment surface. So although the leaves may be relatively higher or lower dependent on leaf positions the virtual sensor is not moved up or down. The water optical properties within the canopy were fixed as a typical set of reef lagoon inherent optical properties (Hedley & Enríquez, 2010), while in later analyses the overlying water column optical properties were variable (see below). Fixing the within-canopy IOPs was necessary for computational efficiency; the error introduced will be small and insignificant compared to other factors.

Since the canopy model is three-dimensional it requires a directional light field on the top of the canopy (Fig. 1). This was provided by generating bottom of atmosphere direct and diffuse irradiances with libRadtran (Mayer & Kylling, 2005), combining these with the sky model of Grant, Heisler, and Gao (1996) and propagating this through a plane-parallel water column model (PlanarRad, www.planarrad.com, functionally similar to HydroLight, Mobley, 1994). Since the objective was to model diffuse reflectance of the canopy the purpose of the sky and water column modelling is to provide a reasonable directional distribution of radiance at the bottom of the water column. The canopies are not actually Lambertian reflectors (Hedley & Enríquez, 2010) but to develop the image analysis algorithm presented later it is required to treat them as such. The modelling was repeated for depths of 1, 5 and 10 m, and for solar zenith angles of 26° and 56° (Table 1) to demonstrate if the canopy bi-directional reflectance function and incident light field produced any variation in the diffuse top of canopy reflectance, and to find the mean diffuse reflectance over a range of realistic light fields. The solar zenith angles corresponded to solar midday and 3 h either side of midday at the Florida Bay field site. The effects of relative solar azimuth were considered out of scope for this study, so the modelled light fields were azimuthally averaged.

2.3. Functional form of spectral reflectance

For each of the model runs covering LAI from 0.1 to 10 the above-canopy diffuse spectral reflectance, $R(\lambda)$, was calculated. These results described the general pattern of variation of reflectance with LAI, but with additional perturbations due to canopy structure and the other factors in Table 1. From previous work (Hedley & Enríquez, 2010; Hill, Zimmerman, Bissett, Dierssen, & Kohler, 2014) it was anticipated that at each wavelength the basic relationship between LAI and reflectance would be a negative exponential of the form,

$$R(\lambda) = A(\lambda)\exp(-k(\lambda) \times \mathrm{LAI}) + B(\lambda) + \varepsilon(\lambda). \quad (1)$$

At each wavelength reflectance decreases monotonically as LAI increases. The effect is less as LAI becomes large and an asymptotic reflectance is reached in very dense canopies where adding more leaves has no further effect on reflectance. The values A, k and B for each

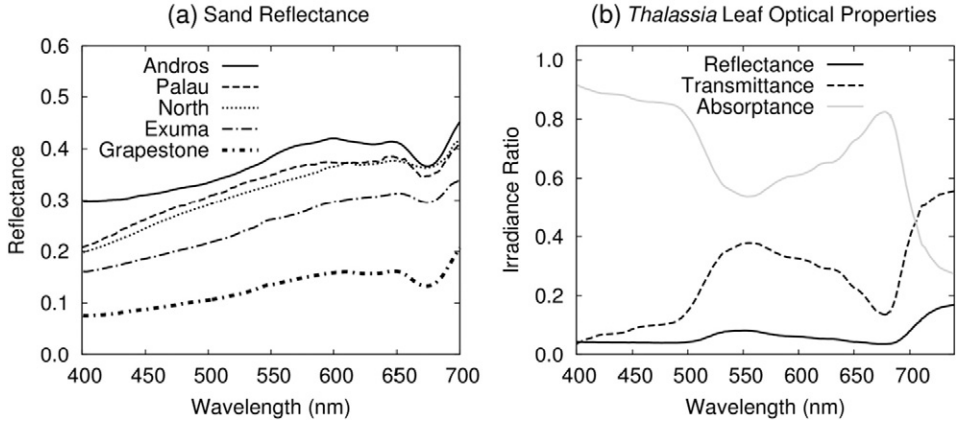

Fig. 3. (a) The five sand reflectance spectra used in the modelling (Table 1), (b) the reflectance, transmittance and absorptance of *Thalassia* leaves, replicated from Zimmerman (2003).

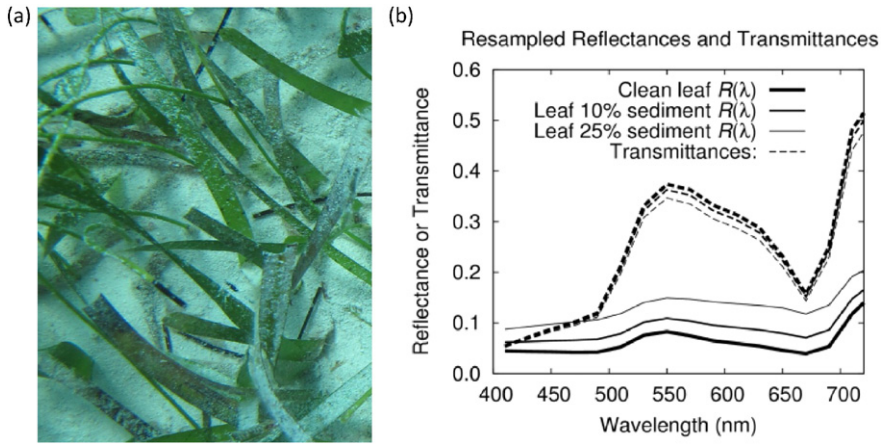

Fig. 4. (a) Photograph showing sediment or calcareous epiphyte covered *Thalassia* leaves at the test site, (b) spectral reflectance and transmittance of leaves for the treatments of clean and 10% and 25% sedimented (Table 1). Spectra in (b) are resampled to 16 bands of 20 nm interval, and are as used in the canopy model (Fig. 1).

wavelength were estimated by optimally fitting this function to the $R(\lambda)$ from the model runs. The residual error for each model output is represented by $\varepsilon(\lambda)$, which can be thought of as a spectral vector, added onto the function expressed by A, k and B and being different for each canopy instance. The aim was to make a simplified function to capture this variation, of the form,

$$R(\lambda) \approx R_{\text{canopy}}(\text{LAI}, e_1, e_2, \ldots, \lambda) \tag{2}$$

where the top of canopy reflectance is a function of LAI, and one or more error terms, e_1, e_2, etc. encompass the majority of the variation in the residual spectra $\varepsilon(\lambda)$. To do this the LAI range was broken down into intervals of 0.5 (i.e. 0.5 ± 0.25, 1 ± 0.25, etc.) and a principal components analysis (PCA) applied to the spectra $\varepsilon(\lambda)$ in each interval. Typically it was found that a single scalar parameter e_1, multiplied by the most significant principal component vector was enough to encompass virtually all of the spectral variation in $\varepsilon(\lambda)$ and reconstruct the original reflectances to within a few percent (Fig. 5). The range of the scaling factor e_1 required to reconstruct the range of $R(\lambda)$ in each interval was deduced and the offset and scaling required to allow e_1 to be expressed ranging from 0 to 1 was calculated, i.e. $e_1 \rightarrow e_1[0\text{–}1] \times (e_{1\max} - e_{1\min}) + e_{1\min}$. From the results at each LAI interval the residual and $e_{1\min}$ and $e_{1\max}$ at a specific LAI were calculable by linear interpolation between the interval centres. The result is a two-parameter model for above canopy spectral diffuse reflectance,

$$R(\lambda) \approx R_{\text{canopy}}(\text{LAI}, e_1, \lambda) \tag{3}$$

in which e_1 has no meaning other than it ranges between 0 and 1 and encompasses almost all of the spectral variation induced by unknown factors of canopy structure. Two sets of simplified functions were derived for the sensitivity analysis: 1) Assuming clean leaves and incorporating only the canopy structural variations of Fig. 2; 2) incorporating structural variations and the different levels of sediment coverage of leaves of 0, 10 and 25%. The individual functions are derived using results for a single sediment reflectance only, as in this application it was assumed that sediment reflectance does not vary across a site.

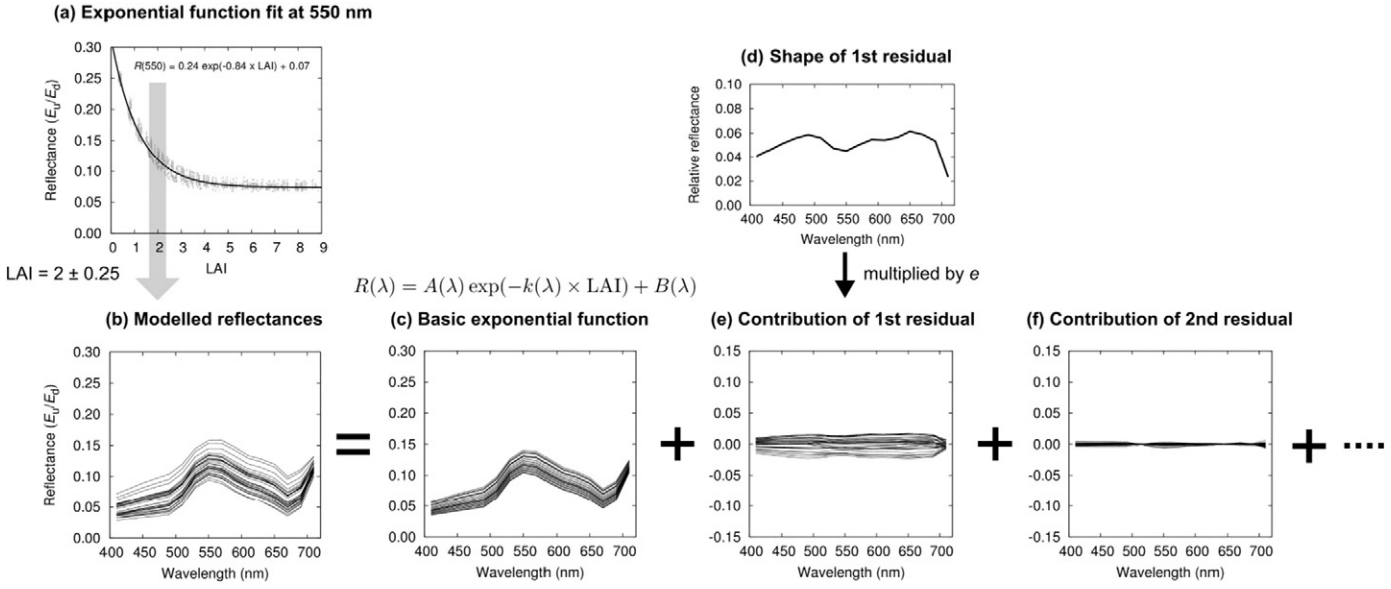

Fig. 5. Derivation of the simplified reflectance model from the canopy model reflectances. (a) An exponential model fit captures the LAI dependence, then at each 0.5 LAI interval (b) the source data is decomposed into (c) the LAI function and (d, e, f) successive smaller residual spectra. A single residual term is enough to reconstruct the original reflectances to within a few percent.

2.4. Model inversion method for image processing

In general, physics-based methods for shallow water remote sensing establish a forward model for predicting the above-water water-leaving remote sensing reflectance, $R_{rs}(\lambda)$, based on parameters of the water column and bottom reflectance. This model can then be 'inverted' per image pixel by the use of successive approximation or look-up tables for spectral matching, to find the best estimate of the input parameters that give rise to the measured water-leaving reflectance (Dekker et al., 2011). A typical form of the forward model is,

$$R_{rs}(\lambda) \approx f(P, G, X, H, R(\lambda), \lambda) \quad (4)$$

where the remote sensing reflectance at wavelength λ is given by some function *f*, dependent on the amount of phytoplankton (*P*), dissolved organic matter (*G*), backscatter (*X*), depth (*H*), and bottom reflectance, $R(\lambda)$. This idea was originally developed by Lee et al. (1998, 1999), and the equations embedded in the function *f*, and as were used here, are given in summary in Hedley et al. (2009). In most applications the bottom spectral reflectance $R(\lambda)$ is chosen from a spectral library of in situ reflectance measurements of different bottom types or may be a linear mix of two or more such spectra (Dekker et al., 2011). Then in the inversion the optimal bottom reflectance and mixing parameter is estimated along with estimates of *P*, *G*, *X* and *H* by least-squares minimisation of difference between $R_{rs}(\lambda)$ and the image reflectance in each pixel. Here, in order to estimate *Thalassia* LAI, $R(\lambda)$ was substituted by Eq. (3) giving,

$$R_{rs}(\lambda) \approx f(P, G, X, H, \mathrm{LAI}, e_1, \lambda). \quad (5)$$

By this method the LAI and the error terms can be estimated by the spectral matching procedure along with the depth and water column optical properties. The error term gives the degree of freedom to the model that encompasses the uncertainties due to canopy structure and position, and leaf sediment coverage if that is included.

The final step required to fully express the uncertainty in the inversion at each image pixel was to incorporate image and environmental noise. Eq. (5) is designed to capture the factors that cause variation in the water-leaving radiance. i.e. factors below the water surface. However, reflection from the top of the water surface, atmospheric fluctuations and sensor noise also cause spectral variation. This is true even if corrections such as sun-glint correction are applied (Hedley et al., 2005) because such corrections are not perfect and some variation will remain. This noise-equivalent perturbation of R_{rs}, $\mathrm{NE}\Delta R_{rs}$ (Brando et al., 2009), was estimated by taking the covariance matrix over a deep water area, where the subsurface factors expressed in Eq. (5) are assumed to be constant or have no effect on the water leaving reflectance. This covariance matrix was then used to simulate the environmental noise. In our method each pixel was inverted 20 times with a different simulated noise term added on, giving 20 estimates of the depth, LAI, and the other parameters in Eq. (5). From these 20 estimates the 90% confidence interval of each parameter were deduced at each pixel, being the result of both the environmental above-water uncertainties and the uncertainty due to canopy variations expressed by e_1. Further details on this uncertainty propagation methodology can be found in Hedley et al. (2010), Hedley, Roelfsema, Koetz, et al. (2012) and Garcia, Fearns, and Mckinna (2014).

In both the image and sensitivity analyses the Levenberg–Marquardt (L–M) algorithm was used to perform the actual spectral matching inversion of Eq. (5) (Wolfe, 1978). The possible range of the parameter values were P [0, 0.06]; G [0, 0.1]; X [0, 0.02]; H [0, 20]; LAI [0, 6]; e_1 [0, 1] (Table 2). The parameter limits of the water optical properties, *P*, *G* and *X*, were chosen by reference to a field dataset of inherent optical properties in reef lagoons (Hedley, Roelfsema, Phinn, & Mumby, 2012). Eq. (5) was evaluated at a wavelength resolution corresponding to a subset of the bands of the hyperspectral data described below, specifically 107 bands with centres from approximately 410 to 710 nm. The canopy model results and other internal spectrally tabulated data, such as phytoplankton optical properties (Lee et al., 1998) were resampled to these wavelengths by linear interpolation. To avoid local optima in the L–M inversion each inversion was repeated five times with a random parameter start point and the best matching solution of the five taken. It was verified by inspection that this gave consistent results implying the inversion was not hampered by local optima.

2.5. Sensitivity analysis

Given the forward model of Eq. (5) and a method for estimating above-surface image noise, the first question asked before application to image data, was what are the fundamental uncertainties that arise simply from the possibility of multiple solutions of Eq. (5)? That is, assuming the model is a perfect representation of reality how do the uncertainties propagate to the estimation of LAI and depth? This was investigated by self-inverting the model using the same image noise covariance matrix as described above. That is, Eq. (5) was used to model $R_{rs}(\lambda)$ for a given set of input parameters, a random spectral noise term was added and Eq. (5) was then inverted by spectral matching and the estimated parameters compared to the ones used to generate the $R_{rs}(\lambda)$. A sensitivity analysis for LAI estimation at three depth ranges was conducted, 1 ± 0.5 m, 5 ± 0.5 m and 10 ± 0.5 m, using a version of Eq. (5) that in one case included only clean leaves, and in the second case was based on the clean leaves and the 10% and 25% sediment covered leaves (Table 2). A sensitivity analysis for depth estimation was also conducted where depth ranged from 0 to 20 m and LAI ranged from 0 to 6. In each case 2500 spectra were generated with *P*, *G* and *X* fixed at the centre of their ranges, but with depth (*H*), LAI and e_1 randomly drawn from a uniform distribution over the specified ranges (Table 2). In the inversion all parameters were freely variable over their full range (Table 2). The spectral bands of the modelling and the noise model covariance matrix were the same as used in the image analysis described in the next section. The analysis was performed only for the North sand reflectance, again to correspond to the image analysis.

2.6. Application to imagery and comparison to field data

The model inversion method was tested on hyperspectral airborne imagery acquired by the Portable Remote Imaging Spectrometer

Table 2
Structure of the sensitivity analyses in terms of the parameter range of simulated spectra and the range used in the inversion. For all analyses the inversion has the same degrees of freedom as the image analysis. The modelled spectra are limited to specific cases, e.g. to investigate LAI estimation at specific depths. All four analyses were repeated for canopies of clean leaves and canopies with variable level of sediment on leaves from 0 to 25%. Parameters are: *P*, absorption coefficient due to phytoplankton at 440 nm; *G*, absorption coefficient due to CDOM at 440 nm; *X*, particulate backscatter at 500 nm modified due to solar and view geometry (Lee et al., 1999); *H*, depth in m; and LAI and e_1, canopy parameters defining the bottom reflectance.

Analysis	Forward modelling						Inversion					
	P	*G*	*X*	*H*	LAI	e_1	*P*	*G*	*X*	*H*	LAI	e_1
LAI, 1 m	0.03	0.05	0.01	0.5–1.5	0–6	0–1	0–0.06	0–0.1	0–0.02	0–20	0–6	0–1
LAI, 5 m	0.03	0.05	0.01	4.5–5.5	0–6	0–1						
LAI, 10 m	0.03	0.05	0.01	9.5–10.5	0–6	0–1						
Depth	0.03	0.05	0.01	0–10	0–6	0–1						

(PRISM) instrument (Mouroulis et al., 2013) in Greater Florida Bay, January 2014 (Dierssen, Chlus, & Russsell, 2015). PRISM is a push-broom imager covering 350–1050 nm with spectral resolution of ~3.1 nm (Mouroulis, Green, & Wilson, 2008). A set of flight lines were collected coincidental with a series of in situ LAI and benthic reflectance survey transects, at an altitude such that pixels were approximately 1 m × 1 m. LAIs were estimated at 2 m intervals along transects of 10–25 m by counting shoots in 20 × 20 cm quadrats, and measuring seagrass leaf length and width from samples harvested from the site. Benthic spectral reflectance was also recorded at the sample points utilising a submersible field spectrometer fitted with a fibre-optic cosine collector. Upwelling spectral planar irradiance $E_u(\lambda)$ was divided by a near-simultaneous measurement of downwelling spectral irradiance $E_d(\lambda)$ taken at the same depth and distance from the canopy. In the results these benthic reflectances as a function of LAI are used as an intermediate validation step. Survey points were located in the imagery by a combination of GPS measurements and notes on the local pattern of seagrass density, with survey lines starting on bare sand for example.

Both *T. testudinum* and the spectrally and physically distinct *Syringodium filiforme* were present in the area, and their separate LAI contributions were determined. Since the scope of the model and validation is *Thalassia*, only the data from *Thalassia* dominated areas were used, where the percentage of *Syringodium* with respect to LAI was less than 25% (extension of the method to include *Syringodium* is discussed later). After this quality control screening, coincidentally all the remaining data was contained within a single flight line and was based in two areas: two data points in approximately 1.5 m depth and eleven data points at around 7.8 m depth. The in situ estimated LAIs ranged from 0 to 3, canopy heights were between 12 and 21 cm. The spatial resolution of the flight line was approximately 1 m.

Inherent optical properties of the water were measured at several stations during image acquisition with an instrument ensemble including a WET Labs AC-S, an AC-9 with 0.2 μm filters and BBFL2 backscatterometer. This data was processed after image analysis, and so has only been used for results comparison and not for calibration of the algorithm. In the application of the method the same variable range of IOPs was used for model inversion as shown in Table 2, which are generic ranges and not a site-specific calibration. Total and particulate absorption and particulate backscatter were estimated from the instruments according to standard protocols described in Sullivan, Twardowski, Donaghay, and Freeman (2005); Sullivan et al. (2006); Twardowski and Donaghay (2001); Twardowski, Sullivan, Donaghay, and Zaneveld (1999) and Zaneveld, Kitchen, and Moore (1994). A point of note is that the CTD on the instrument package failed, so estimates of temperature and salinity required for corrections were made using data from the routine sampling locations of the Keys Marine Laboratory.

The hyperspectral imagery was initially atmospherically corrected and converted to $R_{rs}(\lambda)$ using a modified version of the ATREM radiative transfer model to account for Rayleigh scattering, aerosol scattering and absorption effects from atmospheric gases (Gao & Davis, 1997). Sun-glint was corrected per-pixel by use of the Rayleigh-corrected reflectance at 980 nm (Mouroulis et al., 2013). Following the algorithmic atmospheric correction a vicarious calibration adjustment was applied based on above-water spectral reflectance measurements taken over sand areas, co-incidentally with the image acquisition. This data was collected with an ASD FieldSpec 4 with an 8.5° fore-optic, and utilising a grey Spectralon reflectance panel as a reference, following methods outlined in Dierssen et al. (2010). The vicarious adjustment consisted of a spectrally flat scaling, since the spectral shape agreed well but the atmospherically corrected data was overall too bright in comparison to the above water measurements. The solar and view zenith angles are also required by the water column model (although not shown in Eqs. 4 and 5). The above-surface solar zenith angle was computed from the acquisition time and location as ~30°, the field data sites were located close to the flight-line edge implying a view zenith angle of ~14°.

An approximately 100 m × 100 m segment of the hyperspectral imagery containing the data points at 7.8 m depth and range of seagrass density was processed with the inversion algorithm, as was a smaller area containing the two points at approximately 1.5 m depth. Processing occurred in exactly the same manner as the previously described sensitivity analysis (with parameter ranges as in the right hand side of Table 2). The North sand reflectance was used (Fig. 3) since the empirical data and observation indicated that a bright calcium carbonate sand reflectance was appropriate. For comparison, both the canopy model using clean leaves and the model that included variation due to sediment covered leaves were used; photographs of the sample points indicated that sediment coverage was common (Fig. 4). A deep water area at the end of the flight line was used to characterise the above-surface noise covariance matrix, and for each pixel 20 noise perturbed inversions were performed to provide the mean results and 90% confidence intervals for the parameters of interest, in particular LAI and depth.

3. Results and discussion

3.1. Above canopy diffuse reflectance as function of canopy structure and illumination

As expected, for clean leaves, canopy reflectance at all wavelengths decreased approximately exponentially with increasing LAI (Fig. 6), all the sediment reflectances were brighter than the reflectance of seagrass leaves (Fig. 3) so this pattern was consistent but more pronounced with brighter sediments. The saturation of reflectance at high LAIs, where increasing LAI no longer effects canopy reflectance, is a well described feature of vegetative canopies in general (Knyazikhin et al., 1998). Fig. 6 implies that for *Thalassia* with clean leaves, canopy LAIs above around 4 cannot be distinguished by remote sensing. For *Thalassia* an LAI of 4 is at the upper limit of what could be expected, but for species such as *P. oceanica* LAIs of 12 or higher have been reported (Olesen, Enriquez, Duarte, & Sand-Jensen, 2002).

Variable canopy structure and illumination contributed to variation in canopy reflectance but not always systematically. Restricting the discussion to clean leaves (Fig. 6), shorter leaved canopies tend to be brighter than longer leaved canopies at the same LAI, presumably because more underlying sediment can be seen between the leaves (Fig. 6b, see also Fig. 2, leaf length axis). The effect is most pronounced at LAIs of 2 to 3, at very high LAIs the canopy is densely packed regardless of leaf length and the reflectance has low variation (Fig. 6b, high LAI). Similarly, for mid-range LAIs relatively upright leaf positions open up the view of the sediment and brighten the canopy (Fig. 6d). This effect was less systematic than leaf length, because 'upright' and 'flattened' are subjective categories and not strictly delimited. Nevertheless the observation is consistent with the model of Zimmerman (2003) and Hill et al. (2014) that indicated *Thalassia* canopy irradiance absorption increases with leaf bending angle. If these canopy structure uncertainties are assumed to be representative of the variation in real canopies at a given site, then a reflectance of ~0.08 at 630 nm could represent a canopy LAI anywhere from 2 to 3.5 (Fig. 6b). However there are two caveats to this interpretation: 1) this range of leaf length distributions and positions may not be present at a single site; 2) although the pattern seen at 630 nm (Fig. 6) is the same at other wavelengths, the reflectances considered spectrally may have more discriminatory power than at individual wavelengths (note that a wavelength of 630 nm was chosen for Fig. 6 because there is a large difference between leaf reflectance to sand reflectance at that wavelength).

With respect to illumination conditions, varying the depth introduced no systematic variation in canopy diffuse reflectance (Fig. 6c) but varying the solar zenith angle did (Fig. 6a). The variation in solar zenith angle reveals a BRDF effect: canopies with LAI less than 3 are slightly darker when illuminated at an increased angle, but for canopies with LAI greater than 5 the situation is reversed (Fig. 6a). Solar zenith angle

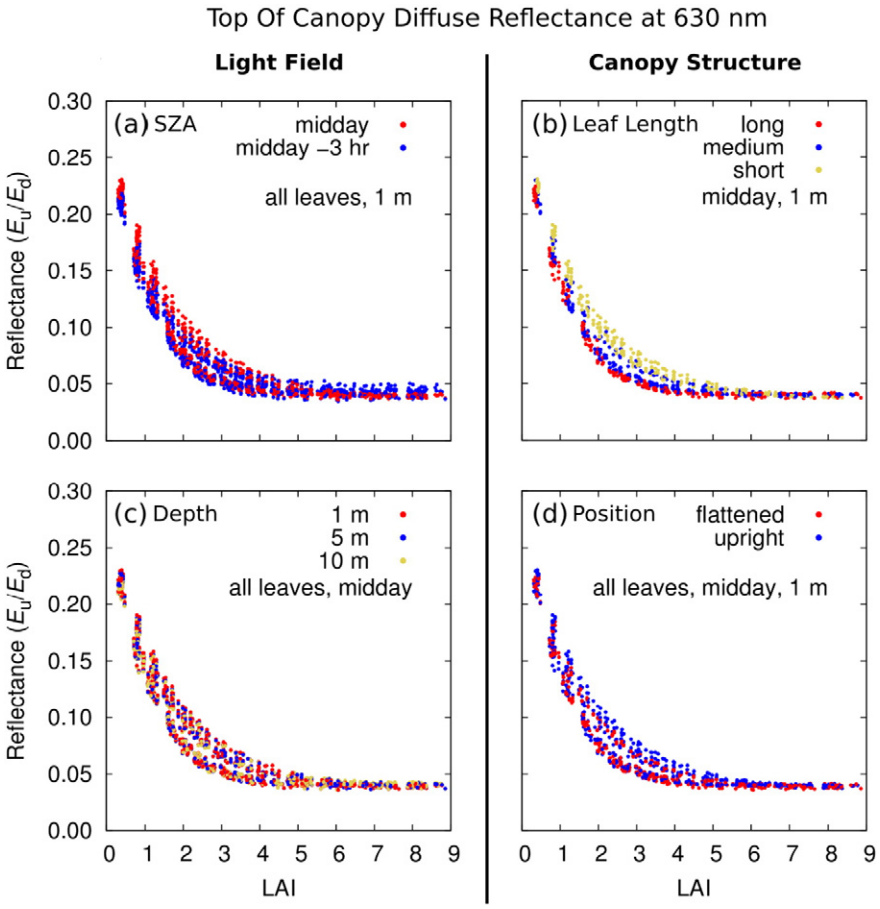

Fig. 6. Effect of individual factors inducing variation in the relationship between LAI and top of canopy diffuse reflectance at 630 nm. All plots are for clean leaves and North sediment reflectance. (a) Effect of solar zenith angle of 26° (mid-day) versus 56° (mid-day ±3 h) over all canopy structures at 1 m; (b) Effect of leaf length distribution for all canopy positions at 1 m at midday (c) Effect of depth for all canopy structures at midday (d) Effect of canopy position for all leaf length treatments at midday and 1 m depth. (a) and (c) together show effects due to variable directional nature of the light distribution incident on the canopy while (b) and (d) are both effects of canopy structure.

variation was the only treatment on clean leaves that introduced noticeable variation in reflectance at high LAIs (Fig. 6a, high LAI). Hence some component of the BRDF is a function of the vegetative canopy structure alone and is independent of the visibility of the underlying sediment. BRDF effects in modelled *Thalassia* canopies been demonstrated previously (Hedley & Enríquez, 2010), but further investigation of their variation with LAI may be useful. Increase in depth will increase the diffuse nature of the incident light field, but this will be a weaker interaction with the BRDF than illumination angle and so has little systematic effect on canopy diffuse reflectance (Fig. 6c). The consequence of the illumination results is that 1) it is appropriate to apply a single benthic reflectance at different depths — as is done in the algorithm presented here, but 2) it may be an improvement to parameterise that benthic reflectance for solar zenith angle. Here, we effectively encompass that variation as an unknown into the method. In practice, we know the solar zenith angle at the time of image acquisition; therefore a future improvement could be to make use of that information in the benthic canopy reflectance function.

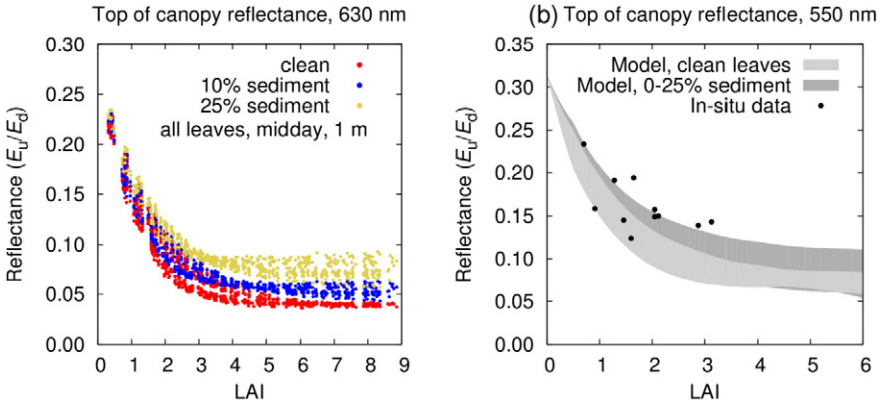

Fig. 7. (a) Effect of sediment on leaves on top of canopy diffuse reflectance at 630 nm. Results are for North sediment reflectance and all canopy structures at mid-day at 1 m depth. (b) Comparison of simplified canopy model function for clean leaves and sediment covered leaves, and field measurements of top of canopy reflectance at 550 nm.

3.2. Sediment coverage on leaves

Incorporating sediment reflectance into the leaf reflectance to simulate sediment coverage levels of 10% and 25% increased the leaf reflectance and consequentially canopy reflectance (Fig. 7a). The effect was clearer for LAIs above 3. For low LAIs a part of the darkening due to the presence of leaves is the shading of the substrate, so leaf reflectance in itself is not the only control of the initial slope of the reflectance function. Shading of the substrate can be observed in Fig. 4a. For LAIs less than around 1.5 the presence of sediment on up to 25% of the leaf surface does not increase the variation in canopy reflectance much beyond that already present from the canopy structural variations (Fig. 7a vs. Fig. 6). For LAIs above 3 however, the possibility of sediment on leaves is a major contributor to variations in canopy reflectance. If a site could have different locations where leaf sedimentation ranges from clean leaves to 25% sediment covered then a reflectance of 0.08 at 630 nm could represent a canopy with any LAI from 2 upwards (Fig. 7a). However, this is based on the assumption that such covariation could exist. For example, biophysical constraints may mean that denser canopies are unlikely to have leaf surfaces with heavy sediment or calcareous epiphyte load.

Fig. 7b shows the range of canopy reflectances, $R(550)$, that can be produced by the simplified functional form of canopy reflectance, i.e. Eq. (5), parameterised for clean leaves only and also for clean and sedimented leaves. In situ reflectances measured with the submersible spectroradiometer are also plotted. It is clear that the model with sediment covered leaves is required to reproduce some of the in situ measured reflectances, which otherwise would be too bright, especially for higher LAIs. There remain two outlying data points that are too bright for their LAI. Photographs of the sample points confirm that coverage of leaves by sediment was ubiquitous and 25% leaf area coverage could be an underestimate in some cases.

3.3. Sensitivity analysis

Noise perturbed self-inversion of the combined canopy reflectance and water column model (Eq. (5)) revealed the fundamental uncertainty in LAI and depth estimation from water leaving reflectance (Fig. 8). The first observation from Fig. 8 is that the distributions of the individual estimates are accurately bounded by the corresponding 90% confidence intervals provided by the algorithm. This verifies that the method for per-pixel uncertainty estimation works as expected. Assuming clean leaves and waters of ~1 m depth, the 90% confidence intervals indicate LAIs of up to 2 can be estimated to within an error of around ± 0.1 (Fig. 8a). Increasing the depth to 5 or 10 m primarily increases the propensity to overestimate the LAI, at 10 m an input LAI of 2 could be estimated as being from 1.5 to 4. The tendency is to overestimate LAI most likely occurs because deeper waters are in general darker due to water column absorption; a dark pixel can be misidentified as a shallower pixel with higher LAI. Conversely, a bright pixel must be low LAI in shallow water; bright pixels have less ways to be produced by alternate situations. This leads to a potential bias toward LAI over-estimation if depth has a wide range.

Uncertainty in LAI estimation is greater when leaves can be covered in sediment or calcareous epiphytes (Fig. 8b). However for LAIs less than 2, the presence of sediment covered leaves does not greatly impair the accuracy of LAI estimations in comparison to clean leaves (Fig. 8b vs. Fig. 8a, LAI < 2). This corresponds to the previous observation that at low LAIs canopy reflectance has a degree of independence from leaf reflectance due to the contribution of shading (Fig. 7a). Hence variation in leaf reflectance is not very important in this region. For both the clean leaf and sediment covered leaf models there is an approximate threshold at LAI greater than 2 where uncertainties in LAI estimation rise rapidly. By an LAI of 4 a maximal uncertainty has been reached, corresponding to the saturation of canopy reflectance (Fig. 6). Note

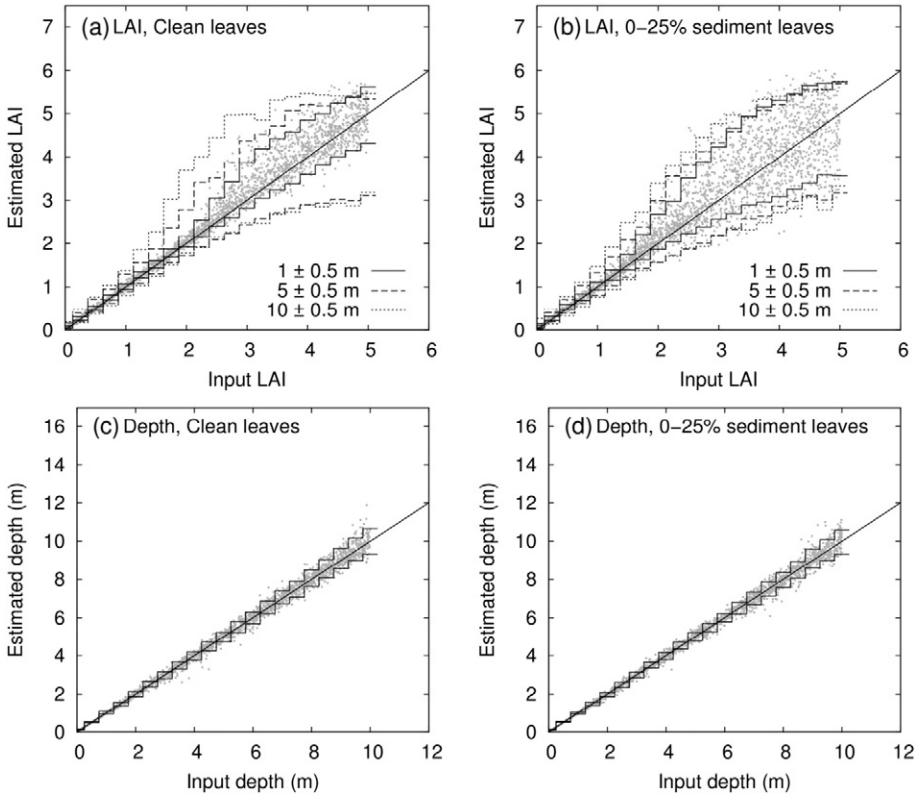

Fig. 8. Model uncertainties estimated by self-inversion with noise perturbed data. (a, b): uncertainties in LAI estimation for depths of ± 0.5 m around 1, 5 and 10 m, lines are inversion algorithm confidence intervals, taken as a mean over the stepped intervals, points show individual inversions results for 1 ± 0.5 m depth. Diagonal is 1:1 line for reference. (c, d): uncertainties in depth estimates for LAIs ranging from 0 to 5. Left panels (a, c) are for a model parameterised for clean leaves only, right (b, d) also include leaves covered in 10% and 25% sediment. Results are for North sediment reflectance only.

that the only reason that the LAI estimate confidence intervals have an upper bound in Fig.8a and b for LAIs greater than 4 is that the inversion is constrained to a maximum LAI of 6. This is equivalent to supplying the a priori information that canopies of LAI greater than 6 do not exist.

Estimation of depth is more robust to uncertainties and image noise than LAI (Fig. 8c and d). With LAI ranging from 0 to 6 and the water column optical properties as listed in Table 2, the sensitivity analysis predicts that depth can be estimated with a fairly consistent ±10% accuracy at least to 10 m. In addition, the result is the same for clean leaves or when the reflectance of leaves varies with sediment coverage (Fig. 8d vs. Fig. 8c). This result occurs because the spectral changes which are the main cues for water depth are present in the spectral profile of water absorption, which is linearly distinct from the reflectance of sand and seagrass (see examples in Hedley, Roelfsema, Phinn, et al., 2012). This explains why physics based methods in general are able to robustly estimate depth even when the associated benthic cover identification may be inaccurate (Dekker et al. 2011; Hedley, Roelfsema, Koetz, et al., 2012).

3.4. Hyperspectral image analysis

The broad pattern of the imagery analysis LAI estimations matched the in situ data well (Fig. 9). Although there were deviations in the LAI estimations at each point these were frequently within the bounds of

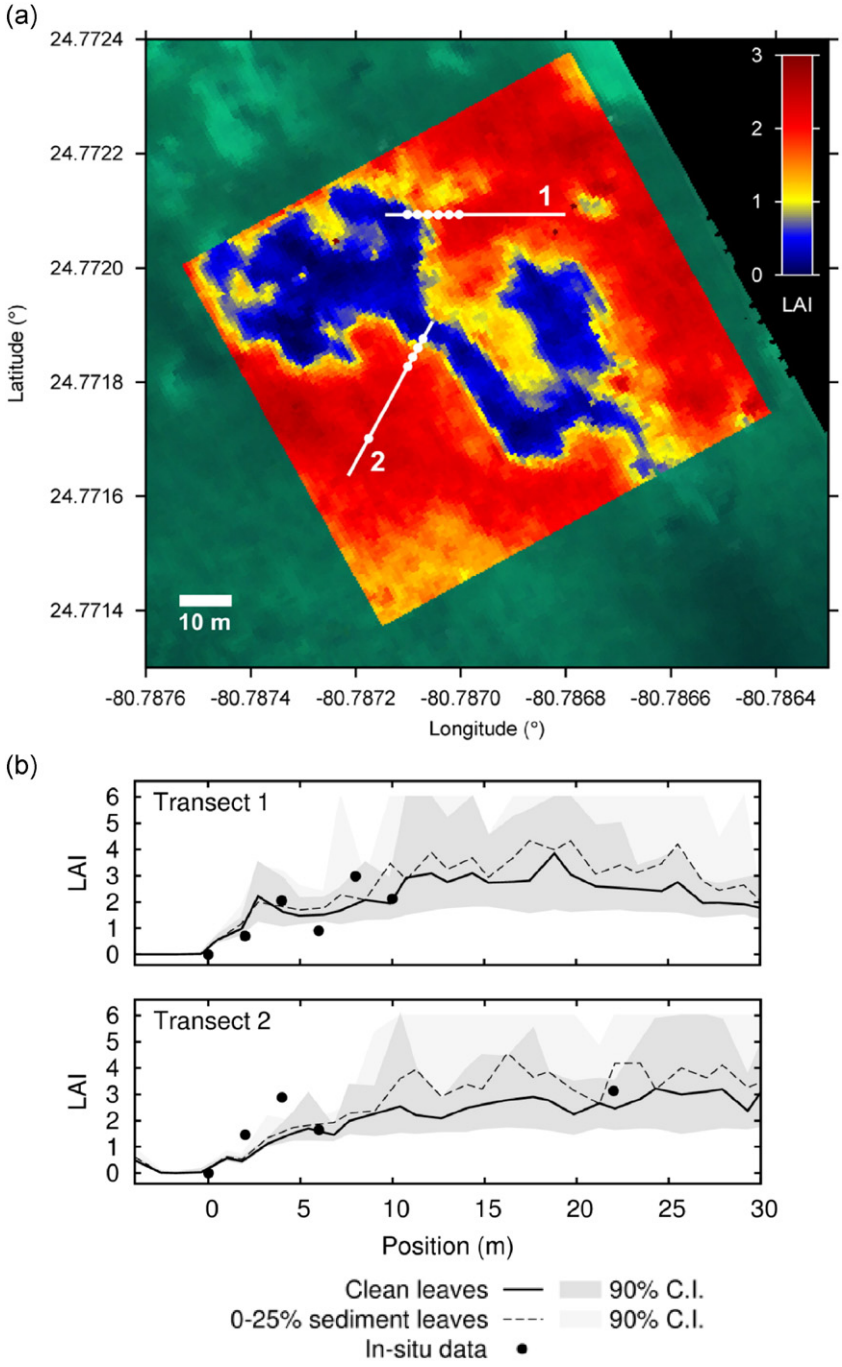

Fig. 9. (a) Inversion algorithm applied to a section of hyperspectral imagery, overlain on an RGB colour composite of three bands. (b) Transects corresponding to the white lines in (a), black dots are in-situ quadrat data, lines are inversion results for the model with only clean leaves and the model with leaves with 0–25% coverage by sediment. Grey areas are 90% confidence intervals from the uncertainty propagation.

the uncertainty propagation (Fig. 10). Both of the field transects at 7.8 m depth started in bare sand, the imagery captures well the increasing LAI as the transects move into denser canopies, and for LAIs up to around 2 the model for clean leaves and sediment covered leaves are not appreciably different (Fig. 9b). This is in line with the previous discussion point; the darkening of the canopy at low LAIs is partly independent of leaf reflectance. The increase in LAI along the transects derived from the imagery is smoother than the in situ data, which increases and decreases point-to-point (Transect 1, Fig. 9b). This underlines the difficulty of working with the very different scales of field data and imagery, the in situ LAIs were determined from 20 × 20 cm quadrats, whereas each image pixel is covering at least 1 × 1 m or more if the adjacency effects of the sensor or water column are considered (Mobley & Sundman, 2003). Collecting data sufficient to precisely assess a seagrass LAI algorithm would be onerous. Given the difficulty of spatial registration (Phinn et al., 2008), LAIs would need to be quantified over areas of at least twice the pixel size. Visual assessment methods can be applied at such scales (Mumby et al., 1997) but are inappropriate because the visual appearance is subject to the uncertainties we wish to assess. The results of Fig. 9 are therefore reasonable, given the limitations of the in situ data.

For estimated LAIs greater than around 2 the propagated uncertainties in the LAI estimation rise rapidly (Fig. 9b). As expected, the model that includes sediment covered leaves has higher uncertainties than the clean leaf model and tends to estimate higher LAIs as LAI increases, consistent with Fig. 7 and the sensitivity analysis (Fig. 8). In all cases the uncertainty is biased in the direction of potentially higher LAIs, for the reasons discussed previously — that the model has more freedom in that direction. A large part of the uncertainty budget in these results is due to basic environmental-sensor noise in combination with the depth of the water (8 m). This can be appreciated from the sensitivity analysis of the clean leaf model (Fig. 8a) where depth of 10 m greatly increases for LAIs greater than 2. The two data points taken from a depth of 1.5 m have very small uncertainties in the LAI estimation (Fig. 10).

While the focus of our method is LAI estimation, the algorithm also estimates depth and water column optical properties. The mean depth of the nine points recorded as being at a site of depth 7.8 m was estimated as 8.54 ± 0.43 m (one standard deviation), which is a statistically significant difference (t-test, $p < 0.05$) and cannot be accounted for by tidal variation since the tide range in the week of data collection was less than 0.7 m (UKHO, http://www.ukho.gov.uk/easytide). However, the 90% confidence intervals on depth from the uncertainty propagation ranged from 7.54 to 10.19, the recorded depth of 7.8 m is within the uncertainty range for five of the nine points. In comparison the sensitivity analysis was slightly more optimistic regarding expected performance, predicting at a depth of 8 m the 90% confidence intervals would be 7.5 to 8.5 m (Fig. 8c, d). In situ depth was not recorded at the individual points, so the deviation may be the result of a depth range at the site. At the shallow site depth was recorded as being approximately 1.5 m and was estimated as 1.48 m at both points with a 90% confidence interval range of 1.35 to 1.58 m. The bathymetric results are therefore as expected for these kinds of methods, being more accurate in shallow waters (Dekker et al. 2011).

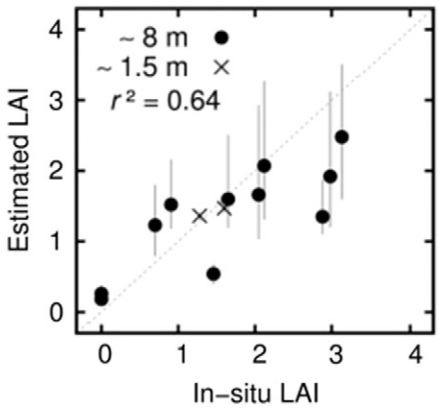

Fig. 10. LAI estimated by remote sensing model for clean leaves versus in-situ measured LAI. Vertical bars are 90% confidence intervals from the uncertainty propagation. • — points from site with depth ~8 m, × — points from site with depth ~1.5 m (on which the error bars are smaller than the symbol).

Over the area depicted in Fig. 9a the estimated water optical properties were consistent and did not vary systematically over light and dark benthic patches, as might be expected to occur with a multiple parameter inversion method. The estimated values were: P (phytoplankton) = 0.0032 ± 0.0010; G (CDOM) = 0.053 ± 0.0035; X (particulate backscatter) = 0.0120 ± 0.0016 (plus–minus is one standard deviation). Table 3 compares the image estimated IOPs to the in situ IOP measurements by the following methods: the G value is the component of the absorption coefficient at 440 nm due to CDOM, $a_g(440)$, available from the filtered AC-9 data; the P value represents absorption due to phytoplankton, or $a_\phi(440)$, which for purposes of comparison can be compared to the measured particulate absorption $a_p(440)$, calculated by subtracting the filtered absorption from the AC-S data; the X value is effectively the particulate backscatter modified to account for non-zero solar and view zenith angles and can be converted to b_{bp} at 500 nm by the expression in Lee et al. (1999).

The two closest IOP stations to the processed area of Fig. 9 were coded 009 and 015, at distances of 1.4 km and 3.8 km respectively, but the data of 015 was obtained within an hour of the image overflight whereas 009 was obtained the previous day. The IOP data of the station close in time (015) matches the image analysis well, total absorption at 440 nm differs by only 20% and particulate or phytoplankton absorption is very low. CDOM absorption and particulate backscatter at 015 are also similar to the image analysis, especially in comparison to station 009 where all values are a minimum of two times greater. While the in situ IOP data is insufficient to make general statements about the method accuracy with respect to IOPs (and this is not he the primary objective of the method) the results suggest the model has good optical closure in all of its sub-components.

3.5. Application to other image sources and scope for improvement

The mapping algorithm has been implemented within a software framework that is sensor-agnostic. All calculations in the forward model can be performed hyperspectrally and convolved to the sensor band relative spectral response (RSR) functions at the point of spectral matching (Hedley, Roelfsema, Koetz, et al., 2012). Application to multispectral satellite data such as Landsat-8 or Sentinel 2 MSI is technically straightforward; the reduced number of bands may increase the uncertainty and under-determine the system but this will be revealed by the uncertainty propagation. Increased uncertainty would be compensated for by free availability of multiple acquisitions (Sentinel 2 having a five-day revisit time at the equator). A time series of points with high uncertainty may have similar statistical power to few points with narrower uncertainties. Further, note that the benefits of hyperspectral data are not necessarily substantial: The accuracy of the bathymetry derived from 17-band hyperspectral data in Hedley et al. (2009) is similar to the resampled five-band analysis of the same data in Hedley, Roelfsema, Koetz, et al. (2012). If the phenomena to be derived are spectrally broad-band and linearly separable, as water column absorption and benthic reflectance are, then fewer wider bands maybe sufficient to capture the major patterns. High quality atmospheric correction of the data is required and may be challenging for these sensors in coastal environments.

Spatial resolutions of 10 to 30 m as provided by sensors such as Landsat, Sentinel 2 MSI or the historical SPOT series will require re-interpretation of the uncertainty estimates. The spatial scale of the canopy modelling is such the canopy reflectance at a scale of 30 × 30 cm is considered representative of a whole pixel. For example, if the canopy is

Table 3
Inherent optical properties measured by in situ instruments at two stations and as estimated by image analysis. Note pure water absorption $a_w(440) = 0.0064\ m^{-1}$ (Pope & Fry, 1997) and total absorption $a = a_w + a_{p/\phi} + a_g$. Error terms are plus–minus one standard deviation, from instrument acquisition cycle repeats for in situ data and over the pixels of the processed area for image data.

Station	Time and date (local time)	Latitude	Longitude	Total absorption	Particulate or phytoplankton	CDOM	Particulate backscatter
				Total $a(440)$	$a_p(440)$ or $a\phi(440)$	$a_g(440)$	$b_{bp}(550)$
	EST	°	°	m^{-1}	m^{-1}	m^{-1}	m^{-1}
009	12:10 13 Jan. 2015	24.7805	−80.7982	0.1540 ± 0.0094	0.0567 ± 0.0065	0.0919 ± 0.0022	0.0167 ± 0.0010
015	11:27 14 Jan. 2015	24.7469	−80.8136	0.0514 ± 0.0063	0.0074 ± 0.0045	0.0396 ± 0.0034	0.0021 ± 0.0006
Image	10:12 14 Jan. 2015	24.7718	−80.7870	0.0630 ± ≈0.0045	0.0032 ± 0.0010	0.0530 ± 0.0035	0.0083 ± ≈0.0011

pushed over by wave action that would be considered homogenous over the whole pixel. While this may be reasonable for 1 m pixels, for pixels of 30 m it is more likely that any individual pixel will contain a mix of canopy states at any moment in time. Therefore the canopy component of the uncertainty budget is likely to be an over-estimate for larger pixels. However, the estimates would be an upper bound of the uncertainty which is preferable to underestimating the uncertainty. In general any uncertainty propagation does require a-priori decisions about the range of situations that can occur at the spatial scale of the imagery and across the area to be analysed. This presents an inevitable chicken-and-egg situation when mapping areas that lack field data.

At larger pixel sizes, LAI is likely to be variable within a pixel and the LAI estimate returned by the algorithm may not correspond to the mean LAI over the pixel. A sensitivity analysis would be recommended to verify that the propagation of uncertainties under conditions of sub-pixel patchiness does not bias the result.

Due to the available validation data, the application presented here was over a much smaller area than the 10's of km^2 scale and up at which remote sensing becomes really useful. At larger scales variation in optical properties of the water would be expected, but the method can accommodate this variation since the optical properties are not fixed but estimated per-pixel, limited by the specified ranges. Variation in water optical properties is potentially a more significant problem for classification or regression approaches. The current limitation of the method is that by design it is restricted to environments that are dominated by *T. testudinum* and the underlying sediment. The presence of other benthic types requires separate processing to exclude them from the analysis. *Thalassia* forms large meadows and for many sites of interest manual delineation may be adequate. In other cases an initial classification or object-orientated image segmentation could be performed (Phinn, Roelfsema, & Mumby, 2012). However within a meadow, and as with the Florida Bay site used here, areas can be composed of multiple species such as *S. filiforme* mixed with *Thalassia*, or contain patches of disconnected *Thalassia* wrack. *Thalassia* wrack in particular is brown due to leaf senescence, collects on the sea bed and appears dark in images. By the current algorithm it would be identified as a high LAI area, but is functionally very different. Extending the method to handle multiple species or benthic types is conceptually straightforward. The canopy model has already been applied to the morphologically very distinct species *Amphibolis griffithii* (Hedley et al., 2014) and can accommodate any seagrass or benthos that can be morphologically characterised. So other bottom types could be modelled in isolation or in mixtures and a simplified canopy reflectance function like Eq. (3) established with one or more additional parameters to describe the composition. Undoubtedly uncertainties will increase and the attempted discrimination may be infeasible, but this would be revealed by the uncertainty propagation. For optimal discrimination between species or disconnected wrack, spectral matching weighted at wavelengths of discriminatory spectral features may be required.

Finally, the upper limits of the uncertainty are bounded by the a-priori designated maximum LAI the algorithm will consider (Fig. 8). This will also govern the best estimates of the LAI for canopies that are dense and close to reflectance saturation. This choice of maximum LAI therefore provides a-priori information that assists the algorithm, but this is not the only a-priori information that could be supplied. For example the highest LAIs for both *T. testudinum* and *Posidonia* spp. are found in shallowest waters (Collier, Lavery, Masini, & Ralph, 2007; Olesen et al., 2002). The uncertainty propagation gives the joint probability distribution of LAI and depth so this a-priori knowledge could be exploited by a Bayesian inference rule to reduce uncertainties, as could any other known constraints on seagrass distribution (Patenaude, Milne, Van Oijen, Rowland, & Hill, 2008).

4. Conclusions

A physics-based remote sensing method for estimating leaf area index of seagrass canopies has been developed. The method is applicable to areas dominated by *T. testudinum*, an important species for organic and inorganic carbon storage forming large meadows in tropical and subtropical coastal environments. The method includes a per-pixel uncertainty propagation including both image noise and uncertainties due to canopy structure. In this paper we have demonstrated the consistency of results from this method across sensitivity analyses and application to hyperspectral imagery with in situ LAI data. The following key points have been noted:

1) Variation in canopy structure such as the distribution of leaf lengths and leaf positions causes variation in canopy reflectance which at a single wavelength can be equivalent to the difference between an LAI of 2 and 3.
2) Remote sensing analysis for estimation of LAI at low LAIs is robust to variation in leaf reflectance because for thin canopies shading is a key aspect of the darkening of canopy reflectance and not only the leaf reflectance itself.
3) Sediment on leaves or bright calcareous epiphytes does cause uncertainties or errors in the estimation of LAI at high LAIs. If the analysis is parameterised to include the possibility of sediment covered leaves with the correct representative probability distribution, the uncertainties may be high but the estimates will be unbiased. Otherwise there could be a systematic over or under-estimation of LAI.
4) For depths approaching 10 m, noise introduced from the water surface upwards, including surface reflectances and sensor noise, dominate the uncertainties in LAI estimation. At increasing depths canopy structure uncertainties are relatively unimportant.
5) Patterns of uncertainty estimated by noise-perturbed self-inversion can be consistent with actual image analysis, but in general this approach is limited by knowledge of the appropriate distribution of input uncertainties. The site of interest has to be well characterised in order to know what range of possibilities exist.
6) BRDF effects introduce a systematic effect of solar zenith angle on canopy reflection. Since solar zenith angle is known this uncertainty

could be eliminated by a parameterised canopy model that includes a dependency on solar zenith angle.

7) Overall, the canopy reflectance model compared well against in situ reflectance measurements, and the remote sensing analysis produced LAI estimates that compared well to field data. Importantly, the method does not require empirical calibration data, but it does require imagery with accurate radiometric correction.

The key strengths of the method are the provision of per-pixel uncertainty estimates and that empirical calibration data is not required. Both features make the method amenable to time series analysis. Application to multispectral data such as Landsat or Sentinel 2 MSI may increase uncertainties but over a time series statistically significant trends may still be detectable: the uncertainty estimates providing a quantitative basis upon which to make this assessment.

Acknowledgements

This work was funded by NASA Ocean Biology and Biogeochemistry Program AWARD #NNX13AH88G. NASA's Earth Science and Technology Office and the Airborne Science Programs have also provided funding for the PRISM instrument. The authors wish to acknowledge the contribution of Bo-Cai Gao at the Naval Research Laboratory and the PRISM team at NASA Jet Propulsion Laboratories including P. Mouroulis, R. Greene, B. VanGorp, I McCubbin and D. Thompson. Field data collection was assisted by A. Chlus, R. Perry, J. Godfrey, and N. De Jesus Rivera from the University of Connecticut and the staff and facilities of the Keys Marine Laboratory. Susana Enríquez of the Universidad Nacional Autónoma de México provided advice and suggestions that have informed some of the comments in this paper.

References

Aragones, L. V., Lawler, I. R., Foley, W. J., et al. (2006). Dugong grazing and turtle cropping: Grazing optimization in tropical seagrass systems? *Oecologia*, *149*, 635–647.

Blakey, T., Melesse, A., & Hall, M. O. (2015). Supervised classification of benthic reflectance in shallow subtropical waters using a generalized pixel-based classifier across a time series. *Remote Sensing*, *7*, 5098–5116.

Brando, V. E., Anstee, J. M., Wettle, M., Dekker, A. G., Phinn, S. R., & Roelfsema, C. (2009). A physics based retrieval and quality assessment of bathymetry from suboptimal hyperspectral data. *Remote Sensing of Environment*, *113*, 755–770.

Burdige, D. J., & Zimmerman, R. C. (2002). Impact of sea grass density on carbonate dissolution in Bahamian sediments. *Limnology and Oceanography*, *47*, 1751–1763.

Collier, C. J., Lavery, P. S., Masini, R. J., & Ralph, P. J. (2007). Morphological, growth and meadow characteristics of the seagrass *Posidonia sinuosa* along a depth-related gradient of light availability. *Marine Ecology Progress Series*, *337*, 103–115.

Dekker, A. G., Phinn, S. R., Anstee, J., Bissett, P., Brando, V. E., Casey, B., Fearns, P., Hedley, J., Klonowski, W., Lee, Z. P., Lynch, M., Lyons, M., Mobley, C., & Roelfsema, C. (2011). Intercomparison of shallow water bathymetry, hydro-optics, and benthos mapping techniques in Australian and Caribbean coastal environments. *Limnology and Oceanography Methods*, *9*, 396–425.

Dierssen, H. M., Chlus, A., & Russsell, B. (2015). Hyperspectral discrimination of floating mats of seagrass wrack and the macroalgae *Sargassum* in coastal waters of greater Florida bay using airborne remote sensing. *Remote Sensing of Environment*. http://dx.doi.org/10.1016/j.rse.2015.01.027.

Dierssen, H. M., Zimmerman, R. C., Drake, L. A., & Burdige, D. (2010). Benthic ecology from space: Optics and net primary production in seagrass and benthic algae across the Great Bahama Bank. *Marine Ecology Progress Series*, *411*, 1–15.

Enríquez, S., & Schubert, N. (2014). Direct contribution of the seagrass *Thalassia testudinum* to lime mud production. *Nature Communications*, *5*, 3835.

Fonseca, M. S., & Cahalan, J. A. (1992). A preliminary evaluation of wave attenuation by four species of seagrass. *Estuarine, Coastal and Shelf Science*, *35*, 565–576.

Fourqurean, J. W., Duarte, C. M., Kennedy, H., Marbà, N., Holmer, M., Mateo, M. A., ... Serrano, O. (2012). Seagrass ecosystems as a globally significant carbon stock. *Nature Geoscience*, *5*, 505–509.

Gao, B. -C., & Davis, C. O. (1997). Development of a line-by-line-based atmosphere removal algorithm for airborne and spaceborne imaging spectrometers. Optical science, engineering and instrumentation '97. *International Society for Optics and Photonics*, 132–141.

Garcia, R. A., Fearns, P. R. C., & Mckinna, L. I. W. (2014). Challenges in detecting trend and seasonal changes in bathymetry derived from HICO imagery: A case study of Shark Bay, Western Australia. *Remote Sensing of Environment*, *147C*, 186–205.

Gobert, S., Sartoretto, S., Rico-Raimodino, V., Andral, B., Chery, A., Lejeune, P., & Boissery, P. (2009). Assessment of the ecological status of Mediterranean French coastal waters as required by the Water Framework Directive using the *Posidonia oceanica* Rapid Easy Index: PREI. *Marine Pollution Bulletin*, *11*, 1727–1733.

Grant, R. H., Heisler, G. M., & Gao, W. (1996). Photosynthetically-active radiation: Sky radiance distributions under clear and overcast conditions. *Agricultural and Forest Meteorology*, *82*, 267–292.

Hedley, J. D. (2008). A three-dimensional radiative transfer model for shallow water environments. *Optics Express*, *16*, 21887–21902.

Hedley, J. D., & Enríquez, S. (2010). Optical properties of canopies of the tropical seagrass *Thalassia testudinum* estimated by a three-dimensional radiative transfer model. *Limnology and Oceanography*, *55*, 1537–1550.

Hedley, J. D., McMahon, K., & Fearns, P. (2014). Seagrass canopy photosynthetic response is a function of canopy density and light environment: A model for *Amphibolis griffithii*. *PloS One*, *9*(10), e111454. http://dx.doi.org/10.1371/journal.pone.0111454.

Hedley, J. D., Harborne, A. R., & Mumby, P. J. (2005). Simple and robust removal of sun glint for mapping shallow-water benthos. *International Journal of Remote Sensing*, *26*, 2107–2112.

Hedley, J. D., Mumby, P. J., Joyce, K. E., & Phinn, S. R. (2004). Spectral unmixing of coral reef benthos under ideal conditions. *Coral Reefs*, *23*, 60–73.

Hedley, J. D., Roelfsema, C., Koetz, B., & Phinn, S. (2012a). Capability of the Sentinel 2 mission for tropical coral reef mapping and coral bleaching detection. *Remote Sensing of Environment*, *120*, 145–155.

Hedley, J. D., Roelfsema, C., & Phinn, S. R. (2009). Efficient radiative transfer model inversion for remote sensing applications. *Remote Sensing of Environment*, *113*, 2527–2532.

Hedley, J. D., Roelfsema, C., & Phinn, S. R. (2010). Propagating uncertainty through a shallow water mapping algorithm based on radiative transfer model inversion. *Proc. Ocean Optics XX*.

Hedley, J. D., Roelfsema, C., Phinn, S., & Mumby, P. J. (2012b). Environmental and sensor limitations in optical remote sensing of coral reefs: Implications for monitoring and sensor design. *Remote Sensing*, *4*, 271–302.

Hill, V. J., Zimmerman, R. C., Bissett, W. P., Dierssen, H., & Kohler, D. D. R. (2014). Evaluating light availability, seagrass biomass and productivity using hyperspectral airborne remote sensing in Saint Joseph's bay, Florida. *Estuaries and Coasts*, *37*, 1467–1489.

Knudby, A., & Nordlund, L. (2011). Remote sensing of seagrasses in a patchy multi-species environment. *International Journal of Remote Sensing*, *32*, 2227–2244.

Knyazikhin, Y., Martonchik, J. V., Diner, D. J., Myneni, R. B., Verstraete, M., Pinty, B., & Gobron, N. (1998). Estimation of vegetation leaf area index and fraction of absorbed photosynthetically active radiation from atmosphere-corrected MISR data. *Journal of Geophysical Research*, *103*, 32239–32256.

Lambers, H., Chapin, F. S., & Pons, T. L. (2008). *Plant physiological ecology* (2nd edition). New York: Springer (604 pp.).

Lavery, P. S., Mateo, M.-Á., Serrano, O., & Rozaimi, M. (2013). Variability in the carbon storage of seagrass habitats and its implications for global estimates of blue carbon ecosystem service. *PloS One*, *8*(9), e73748.

Lee, Z. P., Carder, K. L., Mobley, C. D., Steward, R. G., & Patch, J. S. (1998). Hyperspectral remote sensing for shallow waters, 1. A semi-analytical model. *Applied Optics*, *37*, 6329–6338.

Lee, Z. P., Carder, K. L., Mobley, C. D., Steward, R. G., & Patch, J. S. (1999). Hyperspectral remote sensing for shallow waters, 2. Deriving bottom depths and water properties by optimization. *Applied Optics*, *38*, 3831–3843.

Lyons, M. B., Phinn, S. R., & Roelfsema, C. M. (2012). Long term land cover and seagrass mapping using Landsat and object-based image analysis from 1972 to 2010 in the coastal environment of South East Queensland, Australia. *ISPRS Journal of Photogrammetry and Remote Sensing*, *71*, 34–46.

Lyons, M. B., Roelfsema, C. M., & Phinn, S. R. (2013). Towards understanding temporal and spatial dynamics of seagrass landscapes using time-series remote sensing. *Estuarine, Coastal and Shelf Science*, *120*, 42–53.

Marbà, N., & Duarte, C. M. (1995). Coupling of seagrass (*Cymodocea nodosa*) patch dynamics to subaqueous dune migration. *Journal of Ecology*, *83*, 381–389.

Mayer, B., & Kylling, A. (2005). The libRadtran software package for radiative transfer calculations — Description and examples of use. *Atmospheric Chemistry and Physics*, *5*, 1855–1877.

Mobley, C. D. (1994). *Light and water*. San Diego: Academic Press (608 pp.).

Mobley, C. D., & Sundman, L. K. (2003). Effects of optically shallow bottoms on upwelling radiances: Inhomogeneous and sloping bottoms. *Limnology and Oceanography*, *48*(1 part 2), 329–336.

Mouroulis, P., Green, R. O., & Wilson, D. W. (2008). Optical design of a coastal ocean imaging spectrometer. *Optics Express*, *16*, 9087–9096.

Mouroulis, P., Van Gorp, B., Green, R. O., Dierssen, H., Wilson, D. W., Eastwood, M., ... Franklin, B. (2013). *The portable remote imaging spectrometer (PRISM) coastal ocean sensor: Design, characteristics and first flight results.*

Mumby, P. J., Green, E. P., Edwards, A. J., & Clark, C. D. (1997). Measurement of seagrass standing crop using satellite and digital airborne remote sensing. *Marine Ecology Progress Series*, *159*, 51–60.

Nagelkerken, I., Roberts, C. M., van der Velde1, G., Dorenbosch, M., van Riell, M. C., Cocheret de la Morinière, E., & Nienhuis, P. H. (2002). How important are mangroves and seagrass beds for coral-reef fish? The nursery hypothesis tested on an island scale. *Marine Ecology Progress Series*, *244*, 299–305.

Olesen, B., Enriquez, S., Duarte, C. M., & Sand-Jensen, K. (2002). Depth-acclimation of photosynthesis, morphology and demography of *Posidonia oceanica* and *Cymodocea nodosa* in the Spanish Mediterranean Sea. *Marine Ecology Progress Series*, *236*, 89–97.

Patenaude, G., Milne, R., Van Oijen, M., Rowland, C. S., & Hill, R. A. (2008). Integrating remote sensing datasets into ecological modelling: A Bayesian approach. *International Journal of Remote Sensing*, *29*, 1295–1315.

Phinn, S. R., Roelfsema, C. M., Dekker, A., Brando, V., & Anstee, J. (2008). Mapping seagrass species, cover and biomass in shallow waters: An assessment of satellite multi-spectral and airborne hyper-spectral imaging systems in Moreton Bay (Australia). *Remote Sensing of Environment*, *112*, 3413–3425.

Phinn, S. R., Roelfsema, C. M., & Mumby, P. J. (2012). Multi-scale, object-based image analysis for mapping geomorphic and ecological zones on coral reefs. *International Journal of Remote Sensing, 33*, 3768–3797.

Pope, R. M., & Fry, E. S. (1997). Absorption spectrum (380–700 nm) of pure water. II. Integrating cavity measurements. *Applied optics, 36*, 8710–8723.

Roelfsema, C. M., Lyons, M., Kovacs, E. M., Maxwell, P., Saudners, M. I., Samper-Villarreal, J., & Phinn, S. R. (2014). Multi-temporal mapping of seagrass cover, species and biomass: A semi-automated object based image analysis approach. *Remote Sensing of Environment, 150*, 172–187.

Sullivan, J. M., Twardowski, M. S., Donaghay, P. L., & Freeman, S. A. (2005). Use of optical scattering to discriminate particle types in coastal waters. *Applied Optics, 44*, 1667–1680.

Sullivan, J. M., Twardowski, M. S., Zaneveld, J. R. V., Moore, C. M., Barnard, A. H., Donaghay, P. L., & Rhoades, B. (2006). Hyperspectral temperature and salt dependencies of absorption by water and heavy water in the 400–750 nm spectral range. *Applied Optics, 45*, 5294–5309.

Twardowski, M. S., & Donaghay, P. L. (2001). Separating in situ and terrigenous sources of absorption by dissolved materials in coastal waters. *Journal of Geophysical Research: Oceans, 106*(C2), 2545–2560.

Twardowski, M. S., Sullivan, J. M., Donaghay, P. L., & Zaneveld, J. R. V. (1999). Microscale quantification of the absorption by dissolved and particulate material in coastal waters with an AC-9. *Journal of Atmospheric and Oceanic Technology, 16*, 691–707.

Wabnitz, C. C., Andréfouët, S., Torres-Pulliza, D., Müller-Karger, F. E., & Kramer, P. A. (2008). Regional-scale seagrass habitat mapping in the Wider Caribbean region using Landsat sensors: Applications to conservation and ecology. *Remote Sensing of Environment, 112*, 3455–3467.

Wolfe, M. A. (1978). *Numerical methods for unconstrained optimization*. New York: Van Nostrand Reinhold Company.

Zaneveld, J. R. V., Kitchen, J. C., & Moore, C. C. (1994). Scattering error correction of reflecting-tube absorption meters. In J. S. Jaffe (Ed.), *Ocean optics XII, vol. 2258*. (pp. 44–55). Bergen, Norway: SPIE.

Zimmerman, R. C. (2003). A biooptical model of irradiance distribution and photosynthesis in seagrass canopies. *Limnology and Oceanography, 48*(1, part 2), 568–585.